Probing Topological Charge of Discrete Vortices

Vasu Dev⊙ and Vishwa Pal⊙[*]

Department of Physics, Indian Institute of Technology Ropar, Rupnagar, Punjab, 140001, India

A discrete vortex, formed by a one-dimensional (1D) ring array of lasers, has high output power as compared with a conventional continuous vortex, and therefore has attracted considerable interest due to widespread applications in various fields. We present a method for probing the magnitude and sign of the topological charge (l) of an unknown discrete vortex, by analyzing the interference pattern of a 1D ring array of lasers. The interference pattern of an unknown discrete vortex with $l \neq 0$ is averaged with the interference pattern corresponding to $l = 0$, which gives rise to a variation in the fringe visibility as a function of the laser number (j) in a 1D ring array. The number of dips observed in the fringe-visibility curve is found to be proportional to the magnitude of the topological charge of a discrete vortex. After determination of the magnitude, the sign of $l \neq 0$ is determined by averaging its interference pattern with the interference pattern corresponding to $l = 1$. The number of dips in the fringe-visibility curve decreases by 1 for positive l values and increases by 1 for negative l values. Further, we verify our method against the phase disorder, and it is found that the phase disorder does not influence accurate determination of the topological charge of a discrete vortex. The working principle as well as numerical and experimental results are presented for discrete vortices with topological charges from small to large values. Excellent agreement between the experimental results and the numerical simulations is found. Our method can be useful in applications of discrete vortices especially where conventional continuous vortices have power limitations.

I. INTRODUCTION

Optical beams with orbital angular momentum (also called "optical vortices") have attracted considerable attention due to their applications in a wide range of fields from scientific research to advanced technologies, such as optical communications with increased data-carrying capacity [1,2], optical trapping and manipulation [3–5], microscopy [6], quantum information processing [7,8], remote sensing [9], high-resolution imaging [10], generation of magnetic fields [11], high-harmonic generation [12], astrophysics for cornography [13], and probing the angular velocity of spinning microparticles or objects [14]. An optical vortex possesses a helical wave front that has a phase singularity in the center, resulting in a central dark spot in the transverse field distribution. The optical vortex caries an orbital angular momentum of $l\hbar$ per photon, due to an azimuthal phase term $\exp(il\phi)$, where l is an integer number and is known as the topological charge. Several investigations have been performed on optical vortex beams such as a Laguerre-Gaussian beam [15], a Bessel-Gaussian beam [16], and a circular Airy vortex beam [17]. These beams have continuous intensity around the central dark spot (doughnut shape), and the phase along a contour enclosing the singularity point varies from 0 to $2l\pi$. Because of continuous intensity and phase over the contour, these beams fall in the category of a continuous vortex. A continuous vortex has also been investigated in multimode optical cavities [18], condensed-matter spins [19], superfluid helium [20], and Bose-Einstein condensates [21].

A new class of discrete vortices has also been investigated in different systems, such as in optical lattices of Bose-Einstein condensates [22], photonic structure of light [23–27], coupled lasers [28–30], optical parametric oscillators [31], and fiber arrays [32]. Generally, the discrete vortex consists of a finite number of sites (lasers, or beamlets, or waveguides) in a one-dimensional (1D) ring array, where the intensity in the center is zero and the phase circulates from one site to the next in either a clockwise direction (vortex) or a counterclockwise direction (antivortex). There is steplike behavior of the phase along the contour encompassing the phase singularity [25,30,32]. Discrete vortices are particularly interesting for high-power applications, such as laser ablation, nonlinear frequency conversion, long-range optical communication, material processing, optical trapping and manipulation, and generation of magnetic fields [3–5,11,33–35]. These have been generated by different means, such as coherent combining of laser beams [36–40], where the phases of the laser beams are precisely controlled, phase-locking of lasers [28–30], and nonlinear waveguides [25].

————
*vishwa.pal@iitrpr.ac.in

The applications of an optical vortex are usually associated with its orbital angular momentum, and thus accurately determining the topological charge (magnitude and sign) of an optical vortex is very important. Therefore, exploring simple and effective methods to accurately measure the topological charge of an optical vortex has been a very challenging issue, and there are continuous efforts in this direction. Over the years, several methods have been investigated, and these are broadly classified in two categories: the first type is based on the interference approach, and the second type is based on the diffraction approach. Information on the topological charge is manifested in the intensity distribution when the vortex beam either undergoes diffraction through slits or apertures [41,42] or interferes with another beam (plane wave, or vortex beam, or spherical wave) [43,44]. Therefore, from the diffraction pattern or interference pattern, the topological charge of a vortex beam can be inferred. The interference approaches are mainly based on the Mach-Zehnder interferometer [43–45], Fizeau inteferometer [46], Sagnac interferometer [47], double-slit interferometer [48], multipoint interferometer [49], and Talbot interferometer [50], whereas the diffraction approaches involve an annular aperture [51], a triangular aperture [52], a single slit [41,42], a multipinhole plate [53], gratings [54], metasurfaces [55], etc. Further, some more methods for the detection of the topological charge of a vortex have also been proposed, and are based on conformal mappings [56], multiplane light conversion [57], a mode converter [58], the rotational Doppler effect [59], and a two-dimensional material [60]. The above-mentioned methods rely on detecting the topological charge indirectly by analyzing the changes in the intensity distributions. However, some direct methods for determining the topological charge of a vortex have also been investigated. These are based on directly measuring the phase distribution of a vortex, and the methods include use of a phase-shifting digital hologram [61] or Shack-Hartmann wave-front sensors [62].

Many of these methods have limitations in various forms, such as complexity in the setup, inability to precisely determine high-order topological charges (magnitude and sign), sensitivity to aperture dimensions, and sensitivity to aberrations in the system. Further, most of these methods infer the topological charge of a vortex by propagation and analysis of changes in its intensity distribution. These methods have been applied to continuous systems (continuous vortices). However, it is well known that discrete systems show different propagation behavior, so a natural question arises as to whether the above-mentioned methods can be applied for identification of the topological charges of discrete vortices.

Methods based on direct measurement of the phase distribution of a vortex [61,62] can be useful for determining small values of topological charge of a discrete vortex; however, given the aberrations as well as very small differences in the phases of lasers for large topological charges, these may not be able to precisely determine the high-order topological charges of discrete vortices. Here we present a method for precisely determining the magnitude and sign of topological charges (from small to large values) of discrete vortices based on measuring the interference patterns of a 1D ring array of lasers. More specifically, we average the interference pattern of an unknown discrete vortex ($l \neq 0$) with the interference pattern of a ring array with known topological charge, which gives rise to a variation in the fringe visibility as a function of the laser number, and the number of dips observed in the fringe-visibility curve provides accurate information on the magnitude and sign of an unknown topological charge. Our method is also found to be robust with regard to the phase disorder in a system.

This paper is organized as follows. In Sec. II, we present the working principle of our method with illustrative results. In Sec. III, we describe the experimental generation of a discrete vortex as well as measurement of its interference pattern. In Sec. IV, we present numerical and experimental results on precise determination of topological charges of discrete vortices for different system sizes. Further, results on finding the sign of topological charges (positive or negative) are also presented. The robustness of our method is also verified with regard to the phase disorder. Finally, in Sec. V, we present concluding remarks.

II. WORKING PRINCIPLE

We consider the interference of two waves of intensity I_1 and I_2, one propagating in the z direction and the other propagating at an angle θ with respect to the z axis, in the x-z plane. The fields of these interfering waves can be written as [63]

$$U_1 = \sqrt{I_1} \exp(-ikz) \exp(i\phi_1), \tag{1}$$

$$U_2 = \sqrt{I_2} \exp[-i(k \cos\theta z + k \sin\theta x)] \exp(i\phi_2), \tag{2}$$

where ϕ_1 and ϕ_2 are the phases of the two waves. At the $z = 0$ plane, the resultant intensity after superposition of these two waves can be written as

$$I = |U_1 + U_2|^2 = I_1 + I_2 + 2\sqrt{I_1 I_2} \cos(k \sin\theta x - d\phi), \tag{3}$$

where $d\phi = \phi_2 - \phi_1$. For $I_1 = I_2 = I_0$, we get

$$I = 2I_0 \left[1 + \cos\left(k \sin\theta x - d\phi\right)\right]. \tag{4}$$

The interference intensity distribution consists of straight fringes with maxima and minima whose positions vary with x, and the fringe spacing is given by

$\beta = 2\pi/k \sin\theta = \lambda/\sin\theta$. The locations of minima and maxima can be determined from Eq. (4). For maxima,

$$x_{\max} = \frac{[2m\pi + d\phi]}{k\sin\theta}, \quad m = 0, \pm 1, \pm 2, \pm 3, \ldots. \quad (5)$$

For minima,

$$x_{\min} = \frac{[(2m+1)\pi + d\phi]}{k\sin\theta}, \quad m = 0, \pm 1, \pm 2, \pm 3, \ldots. \quad (6)$$

The positions of the maxima and minima in the interference fringe pattern depend on the value of the relative phase shift $d\phi$. If it is changed, these positions of the maxima and minima shift either to the left or to right with respect to the initial positions. To show this, we consider two Gaussian beams with equal intensity $I_1 = I_2 = I_0$, tilt angle $\theta = 110°$, and $d\phi = 0$, $d\phi = -\pi/2$, or $d\phi = \pi/2$. The interference expressions for these cases can be written as follows:

(i) For $d\phi = 0$,

$$I_{T1} = 2I_0 \left[1 + \cos(0.94kx)\right]. \quad (7)$$

(ii) For $d\phi = -\pi/2$,

$$I_{T2} = 2I_0 \left[1 + \cos(0.94kx + \pi/2)\right]. \quad (8)$$

(iii) For $d\phi = \pi/2$,

$$I_{T3} = 2I_0 \left[1 + \cos(0.94kx - \pi/2)\right]. \quad (9)$$

The interference patterns obtained from Eqs. (7)–(9) are shown in Figs. 1(a)–1(c). As is evident, for all three cases, the interference patterns consist of straight fringes with maxima and minima at different positions. We consider the case of $d\phi = 0$ as the reference interference pattern. A vertical dashed white line marks the position of a fringe with a central maximum [Fig. 1(b)]. For $d\phi = -\pi/2$, the fringes in the interference pattern are shifted towards the right with respect to the reference dashed white line [Fig. 1(a)]. Similarly, for $d\phi = \pi/2$, the fringes in the interference pattern are shifted towards the left with respect to the reference dashed white line [Fig. 1(c)]. The interference pattern is quantified by the fringe visibility $V = (I_{\max} - I_{\min})/(I_{\max} + I_{\min})$ [63], where $I_{\max}$ and $I_{\min}$ are the maximum and minimum values of the time-averaged intensities in the interference pattern. In all three individual interference patterns (for $d\phi = 0$, $d\phi = -\pi/2$, and $d\phi = \pi/2$) the fringe visibility V is found to be 1 [Figs. 1(a)–1(c)]. Note that the fringe visibility is calculated by taking the cross section along a horizontal line drawn through the center of the interference pattern.
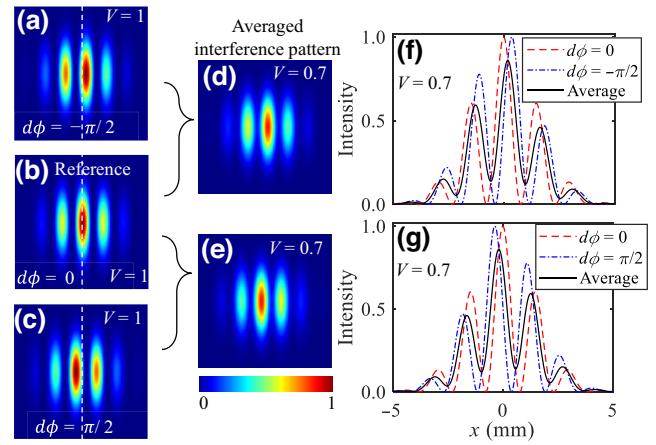

FIG. 1. Interference patterns between two waves with a relative phase shift of (a) $d\phi = -\pi/2$, (b) $d\phi = 0$, and (c) $d\phi = \pi/2$. Averaged interference patterns obtained with superposition of (d) $d\phi = 0$ and $-\pi/2$ and (e) $d\phi = 0$ and $\pi/2$. (f) Intensity cross sections taken along the horizontal axis in (a),(b),(d). (g) Intensity cross sections taken along the horizontal axis in (b),(c),(e).

Further, the averaging between the individual interference patterns is performed by averaging the intensity at the respective spatial coordinates. The expression for the averaged interference pattern can be obtained as follows: (i) For averaging the interference patterns corresponding to Figs. 1(a) and 1(b), we add Eqs. (7) and (8):

$$I_{\text{sum}1} = I_0 \left[2 + \cos(0.94kx) + \cos(0.94kx + \pi/2)\right]. \quad (10)$$

Note that because of averaging, the factor of 2 is dropped. (ii) For averaging the interference patterns corresponding to Figs. 1(b) and 1(c), we add Eqs. (7) and (9):

$$I_{\text{sum}2} = I_0 \left[2 + \cos(0.94kx) + \cos(0.94kx - \pi/2)\right]. \quad (11)$$

The averaged interference patterns corresponding to Eqs. (10) and (11) are shown in Figs. 1(d) and 1(e), respectively. As is evident, when two interference patterns with $d\phi = 0$ and $d\phi = -\pi/2$ or with $d\phi = 0$ and $d\phi = \pi/2$ (each with $V = 1$) are averaged, they produce a resultant interference pattern, where the fringe visibility is found to be reduced ($V = 0.7$) [Figs. 1(d) and 1(e)]. The fringe visibility is again calculated by taking cross sections along the horizontal lines drawn through the center of the interference patterns. This is more clearly shown in Figs. 1(f) and 1(g). Figure 1(f) shows the intensity cross sections taken along the horizontal axis (through the center) in Fig. 1(a) (dot-dashed blue curve), Fig. 1(b) (dashed red curve), and Fig. 1(d) (solid black curve). Similarly, Fig. 1(g) shows the intensity cross sections taken along the

horizontal axis (through the center) in Fig. 1(b) (dashed red curve), Fig. 1(c) (dot-dashed blue curve), and Fig. 1(e) (solid black curve). It is clearly evidenced that the averaged intensity cross section (solid black curve) results in a reduced value of the fringe visibility. Note that averaging the interference patterns corresponding to $d\phi = 0$ and $d\phi = -\pi$ or $d\phi = 0$ and $d\phi = \pi$ results in fringe visibility $V = 0$.

We use this principle of reduction in visibility by averaging the interference patterns to determine the magnitude and sign of the topological charge of an unknown discrete vortex.

III. EXPERIMENTAL ARRANGEMENT

A discrete vortex consists of a finite number of sites (lasers, or beamlets, or waveguides) in a 1D ring array, where the intensity in the center is zero and the phase circulates from one site to the next in either a clockwise direction or a counterclockwise direction [25,28,31,32,38]. The field of a discrete vortex can be given as [39]

$$U(x,y;z=0) = \sum_{j=1}^{N} U_j(x,y;z=0), \quad (12)$$

where U_j denotes the complex field of site j on a 1D ring and can be given as

$$U_j(x,y;z=0) = U_0 \, e^{-\frac{(x-\beta_j)^2+(y-\gamma_j)^2}{\omega_0^2}} e^{i\phi_j}. \quad (13)$$

$(\beta_j, \gamma_j) = \alpha(\cos\delta_j, \sin\delta_j)$ represents the coordinates of each site, $\alpha = d/\sqrt{1-\cos(2\pi/N)}$, $\delta_j = \pi(2j-1)/N$, and $\phi_j = l \times (2\pi(j-1)/N)$, where $j = 1, 2, 3, \ldots, N$. d denotes the center-to-center distance between two neighboring sites. All sites in a discrete vortex have the same amplitude U_0, same beam waist ω_0, and different phase ϕ_j, satisfying the periodic boundary conditions: $U_{j+N} = U_j$. The topological charge (l) of a discrete vortex can be defined as

$$l = \frac{1}{2\pi} \sum_{j=1}^{N} \arg(U_j^* U_{j+1}). \quad (14)$$

In particular, to define a discrete vortex, there should be $N \geq 3$ lasers in a 1D ring array. For a given system size N, the discrete vortex can have a finite number of l values, which are given by the relation $|l| \leq N/2$ [25,29,32]. As opposed to a continuous vortex, a discrete vortex is formed by combining several lasers, and thus does not suffer from output-power limitations.

In our previous work, we showed the generation of a discrete vortex by phase-locking lasers in a 1D ring array inside a degenerate cavity [28,29]. The lasers were coupled by Talbot diffraction, which caused the phase-locking

of lasers in a vortex configuration. However, a discrete vortex with precisely controlled topological charge could not be generated. More recently, an approach has been demonstrated for the controlled generation of a discrete vortex with any topological charge from small to large values, where a spatial Fourier filtering mechanism inside a degenerate cavity phase-locks the lasers in a desired vortex configuration [30]. The spatial Fourier filtering eliminates the undesired phase distributions by introducing extra losses to them, and accordingly a desired phase distribution with minimum loss is obtained at the output of laser cavity.

In the present work, our main goal is to efficiently determine the topological charge (magnitude and sign) of a discrete vortex. To show the proof of the concept of our method, we generated a discrete vortex from a computer-generated hologram using a spatial light modulator (SLM). A schematic of the experimental setup as well as representative results are presented in Fig. 2. We use a phase-only SLM with a screen resolution of 1920×1080 and a pixel size of 8 μm, and a collimated linearly polarized laser beam with a fundamental Gaussian distribution, wavelength $\lambda = 1064$ nm, and beam-waist radius of 10 mm incident normally on the SLM with a beam splitter (BS1). The size of the input Gaussian beam was expanded 10 times by lenses L_1 ($f_1 = 3$ cm) and L_2 ($f_2 = 30$ cm) to illuminate the whole screen of the SLM. On the SLM screen, a computer-generated phase hologram corresponding to a discrete vortex is applied [Fig. 2(b)] (see Appendix A). The phase hologram on the SLM modulates the amplitude and phase of the input Gaussian laser beam, and accordingly the light from the input Gaussian laser beam splits in the form of multiple lasers arranged on a 1D ring array with discrete phase distributions in a vortex configuration. After reflection from the SLM, we obtain modulated light in several orders (see Appendix A), which contains the desired discrete vortex. The desired discrete vortex in the first order is isolated with a spatial Fourier filter (CA1) placed in the middle of a telescope made with lenses L_3 ($f_3 = 30$ cm) and L_4 ($f_4 = 20$ cm). After spatial filtering, we obtain a clean discrete vortex at the back focal plane of L_4. The experimental phase distribution and intensity distribution of a generated discrete vortex are shown in Figs. 2(c) and 2(d), respectively. As is evident, the discrete vortex consists of $N = 10$ lasers (with TEM$_{00}$ fundamental Gaussian mode profiles) in a 1D ring array [Fig. 2(d)], and the lasers possess a discrete phase distribution [Fig. 2(c)] in a vortex configuration. This is identical to a discrete vortex obtained by phase-locking of lasers in a 1D ring array inside a degenerate cavity [28,30].

To determine the magnitude and sign of the topological charge of a discrete vortex, we measured the interference between the lasers using a Mach-Zhender interferometer, as shown in Fig. 2(a). The discrete vortex [Figs. 2(c) and 2(d)] splits into two channels at beam splitter BS2. In one channel (channel 1), the discrete vortex is imaged
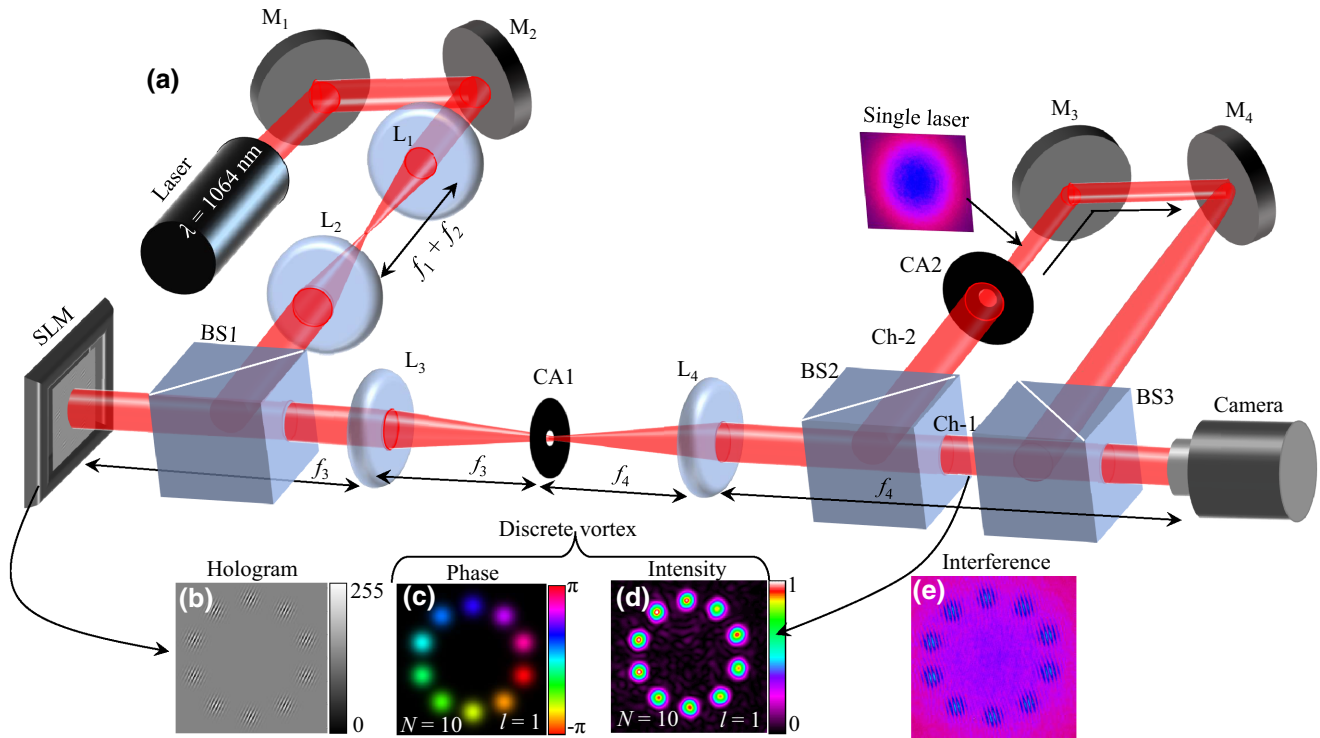
FIG. 2. (a) Experimental arrangement for the generation of a discrete vortex and determining its topological charge (including magnitude and sign). (b) Phase hologram corresponding to a discrete vortex with $l = 1$. (c) Phase distribution of a discrete vortex with $l = 1$. (d) Intensity distribution of a discrete vortex with $N = 10$ lasers. (e) Interference pattern where a single selected reference laser interfered with itself and with all the other lasers. BS, BS2, and BS3, 50:50 beam splitters; CA1, and CA2, circular pinholes; Ch-1, channel 1; Ch-2, channel 2; L_1, L_2, L_3, and L_4, planoconvex lenses with focal lengths $f_1, f_2, f_3,$ and f_4, respectively; M_1, M_2, M_3, and M_4, mirrors; SLM, spatial light modulator.

directly onto a camera. In the other channel (channel 2), a single reference laser is selected with a circular pinhole (CA2) of suitable size, and then its light is expanded such that it fully overlaps and interferes with the light from all other lasers with beam splitter BS3 on the camera. This enables a single selected reference laser to interfere with itself and with all the other lasers. A small tilt [Eq. (2)] between the two channels provides a few interference fringes for each laser [as shown in the interference pattern in Fig. 2(e)], from which the fringe visibility is analyzed. Note that the method requires the calculation of the fringe visibility at spatial positions of lasers in the array, and hence it works well only in the near-field regime of a discrete vortex, where all the lasers are well separated. However, in the far field, the lasers are not separated, and consist of multiple ring structures [30], which is not suitable for fringe-visibility analysis.

IV. RESULTS AND DISCUSSION

To show that our method can efficiently determine the magnitude and sign of the topological charge (from small to large values) of a discrete vortex, we performed several experiments considering different system sizes N and

topological charge from small to large values. The experimental results are supported by numerical simulations. First, we present the results for determining topological charges of discrete vortices, formed with a 1D ring array of $N = 10$ lasers. The results for a discrete vortex with $l = 1$ are shown in Fig. 3.

Figure 3(a) shows the intensity distribution of a discrete vortex, indicating that it consists of a 1D ring array of $N = 10$ lasers with TEM_{00} fundamental Gaussian mode profiles, and each laser has a beam waist of 0.16 mm and is separated by a distance of 0.84 mm (center to center). Figure 3(b) shows the phase distribution of a 1D ring array of $N = 10$ lasers with $l = 0$ (in-phase distribution), indicating that there is no net phase circulation around the center. Figure 3(c) shows the phase distribution of a 1D ring array of $N = 10$ lasers with $l = 1$, indicating the phase circulation around the center (discrete vortex). Note that the intensity distribution of a 1D ring array of lasers for both $l = 0$ and $l = 1$ is the same. Figures 3(d) and 3(e) show the simulated results for individual interference patterns of a 1D ring array of $N = 10$ lasers with $l = 0$ and $l = 1$, respectively, and Fig. 3(f) shows their averaged interference pattern. Figures 3(g) and 3(h) show the experimental results for individual interference patterns of
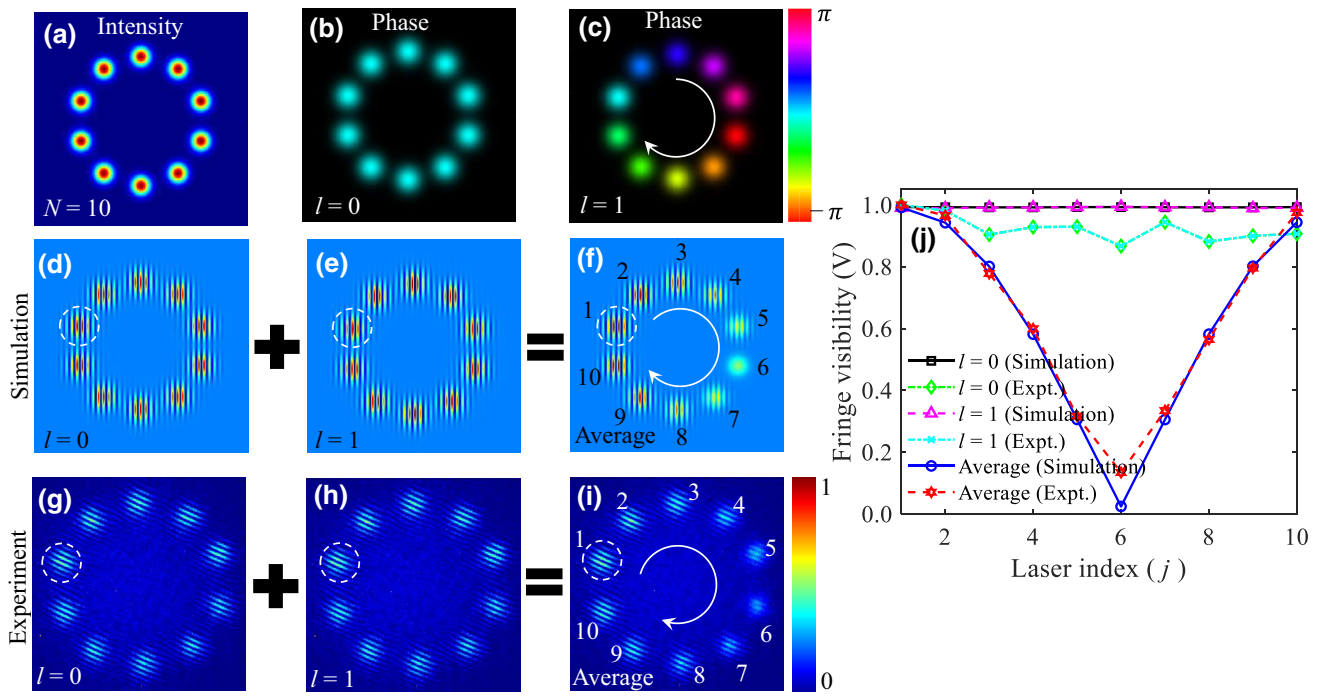
FIG. 3.   Results for a discrete vortex with $l = 1$. (a) Near-field intensity distribution of a discrete vortex formed by a 1D ring array of $N = 10$ lasers. Near-field phase distribution with (b) $l = 0$ and (c) $l = 1$. Interference pattern when a single laser (reference laser, $j = 1$, is denoted by dashed white circle) interferes with itself and with all the other lasers for (d),(g) $l = 0$ and (e),(h) $l = 1$. (f) Average of interference patterns for $l = 0$ (d) and $l = 1$ (e). (i) Average of interference patterns for $l = 0$ (g) and $l = 1$ (h). (j) Variation of fringe visibility as a function of laser index (j). Note that index $j = 1$–10 denotes the laser number in a 1D ring array, as marked in (f),(i).

a 1D ring array of $N = 10$ lasers with $l = 0$ and $l = 1$, respectively, and Fig. 3(i) shows their averaged interference pattern. The averaged interference pattern is obtained by adding the interference patterns corresponding to $l = 0$ and $l = 1$. Note that for averaging, the interference fringes at the respective lasers are added. The dashed white circles in Figs. 3(d)–3(i) mark the locations of a selected reference laser. The individual interference patterns of a 1D ring array of $N = 10$ lasers with $l = 0$ and $l = 1$ are obtained with use of a Mach-Zhender interferometer [Fig. 2(a)], where a selected reference laser interferes with itself and with all the other lasers in the array, which gives rise to interference fringes at all the lasers. As is evident, in the individual interference patterns corresponding to $l = 0$ and $l = 1$, the fringes are uniform at all the lasers, and show no differences between $l = 0$ and $l = 1$ [Figs. 3(d), 3(e), 3(g), and 3(h)]. However, in the averaged interference pattern, the fringes show variation at the lasers [Figs. 3(f) and 3(i)] in a 1D ring array. Particularly, at the reference laser $j = 1$ the fringes appear with clear maxima and minima, and the quality of the fringes degrades monotonically for lasers $j = 2$–6 and then it improves monotonically for lasers $j = 6$–10. This variation in the quality of the interference fringes at all the lasers in the array manifests itself in $l = 1$ of a discrete vortex. This clearly suggests

that the averaging of the interference pattern corresponding to $l = 1$ with the interference pattern corresponding to $l = 0$ enables identification of the topological charge of a discrete vortex.

For a quantitative analysis of these individual and averaged interference patterns [Figs. 3(d)–3(f)], we quantified the interference fringes at all the lasers by calculating the fringe visibility (V) (see Appendix B). The quantified simulated and experimental results are shown in Fig. 3(j), which shows the variation of fringe visibility as a function of laser number ($j = 1, 2, 3, \ldots, 10$) in a 1D ring array. As is evident, for the individual interference patterns corresponding to $l = 0$ [solid black curve with squares (simulation) and dashed green curve with diamonds (experiment)] and $l = 1$ [dashed pink curve with triangles (simulation) and dashed cyan curve with crosses (experiment)], the fringe visibility does not show any variation, and is found to be maximum, $V \approx 1$, at all the lasers in a 1D ring array. Note that because of small intensity differences between the lasers, the experimental visibility is found to be slightly less than 1. However, in the averaged interference pattern, the fringe visibility shows variation as a function of laser index j [shown by the dashed red curve with stars (experiment) and the solid blue curve with circles (simulation)]. For example, the fringe visibility is

found to be maximum ($V = 1$) at laser $j = 1$ and then it decreases monotonically until laser $j = 6$ (minimum V), and then it increases and becomes maximum again at laser $j = 10$. The variation of the fringe visibility in the averaged interference pattern again confirms the manifestation of information on the topological charge of a discrete vortex. Particularly, the observation of a single dip in the fringe-visibility curve can be used to identify $l = 1$ of a discrete vortex.

Further, these variations in the fringe visibility as a function of laser index can be understood by the working principle given in Sec. II (see also Appendix B). In the case of $l = 0$, all the lasers have zero phase ($\phi_j = 0$ and $d\phi_{1,j \geq 1} = 0$, where $j = 1, 2, 3, \ldots, N$), whereas for $l = 1$, the phases of the lasers increase in a clockwise direction [$\phi_j = (j - 1)2\pi/N$ and $d\phi_{1,j \geq 1} = (j - 1)2\pi/N$, where $j = 1, 2, 3, \ldots, N$]. So the reference laser ($j = 1$) in both cases will have interference fringes with maxima and minima occurring at the same positions, and hence averaging does not reduce the fringe visibility. However, for laser $j \geq 2$, we have $d\phi_{1,j \geq 2} = 0$ in the case of $l = 0$ and $d\phi_{1,j \geq 2} = (j - 1)2\pi/10$ ($N = 10$ in the present case) in the case of $l = 1$. Thus, in the interference patterns corresponding to $l = 0$ and $l = 1$, the fringes with maxima and minima will occur at different positions in the same laser $j \geq 2$ [Eqs. (5) and (6)], and as a result of averaging, the fringe visibility is found to be reduced at that laser (Fig. 1, and see Appendix B). The fringe visibility is found to be lowest at laser $j = 6$, where the phase shift $d\phi_{1,6} = \pi$ becomes maximum for $l = 1$ and the fringes are shifted maximally; thus, the averaging results in the lowest value of fringe visibility. For lasers $j = 7$–10 the fringe visibility again increases monotonically. For laser $j = 7$ for $l = 1$, the phase shift $d\phi_{1,7} = 6 \times (2\pi/10)$, and the value of $d\phi_{1,7}$ can also be written as $[2\pi - 4 \times (2\pi/10)]$ or $[-4 \times (2\pi/10)]$. This becomes equivalent to $-d\phi_{1,5}$. The positive and negative values of the same magnitude $d\phi$ produce the same shift of fringes in the interference pattern, as shown in Fig. 1. The magnitude of $d\phi_{1,7}$ is found to be less than that of $d\phi_{1,6}$, so the fringe visibility in the averaged interference pattern at laser $j = 7$ is found to be increased, and it is the same as for laser $j = 5$. Similarly, the fringe visibility for lasers $j = 8$–10 can also be explained (for details, see Appendix B).

In the averaged interference pattern, the variation in the fringe visibility as a function of laser index (j) is characteristics to the value of the topological charge of a discrete vortex, so it serves as the basis for accurate determination of the topological charge. In particular, the observation of a number of dips in the fringe-visibility curve provides information on the topological charge. For example, a single dip in the fringe-visibility curve denotes $l = 1$ [Fig. 3(j)].

The measured interference pattern corresponding to a discrete vortex can also be used to directly calculate the phases of the lasers by analysis of the fringe shifts with respect to a reference laser [28], which can then be used to determine the associated value of the topological charge. However, the direct measurement of phases of lasers may have limitations due to misalignment and aberrations in the system, and for that reason accurate determination of the topological charge of a discrete vortex may not be possible (see Appendix C). In contrast, our proposed method shows high accuracy in determining the topological charge of a discrete vortex.

Further, we determined large values of $l > 1$ in a discrete vortex formed with a 1D ring array of $N = 10$ lasers. The results are shown in Fig. 4. Figures 4(a)–4(f) show the simulated and experimental results obtained by averaging the interference patterns corresponding to $l = 2$, $l = 3$, and $l = 4$ with the interference pattern corresponding to $l = 0$ ($l = 0 + l = 2$, $l = 0 + l = 3$, and $l = 0 + l = 4$). The dashed white circles in Figs. 4(a)–4(f) mark the locations of a selected reference laser, $j = 1$. As is evident, in the averaged interference patterns, the fringes at the lasers exhibit different behavior. The analyzed fringe visibility as a function of laser index (j) corresponding to $l = 2$, $l = 3$, and $l = 4$ is presented in Figs. 4(g)–4(i), respectively, indicating different variations related to the values of the topological charge. This is because the phase distribution of a discrete vortex depends on the value of the l as $\phi_j = l \times (2\pi(j - 1)/10)$ ($j = 1, 2, 3, \ldots, 10$), and accordingly the fringes at the lasers are shifted by different amounts with respect to the fringes for $l = 0$. Thus, averaging of interference patterns for $l \neq 0$ and $l = 0$ results in a different variation in the fringe visibility with the laser index (see Appendix B), and can be used to determine the value of the topological charge. For example, the averaging of interference patterns corresponding to $l = 0$ and $l = 2$ produces two dips in the fringe-visibility curve, confirming $l = 2$ [Fig. 4(g)]. Similarly, the observation of three and four dips in the fringe-visibility curve [Figs. 4(h) and 4(i)] confirms $l = 3$ and $l = 4$, respectively. The simulated and experimental results show excellent agreement.

Further, to show accurate determination of higher-order topological charges of a discrete vortex, we considered a 1D ring array of $N = 30$ lasers. Using the experimental arrangement shown in Fig. 2(a), we generated discrete vortices with $l = 11$–14, and determined their values by averaging their interference patterns with the interference pattern corresponding to $l = 0$. The results are shown in Fig. 5. Figures 5(a)–5(h) show the simulated and experimental results obtained by averaging the interference patterns corresponding to $l = 11$, $l = 12$, $l = 13$, and $l = 14$ with the interference pattern corresponding to $l = 0$ ($l = 0 + l = 11$, $l = 0 + l = 12$, $l = 0 + l = 13$, and $l = 0 + l = 14$). The dashed white circles in Figs. 5(a)–5(h) mark the locations of a selected reference laser, $j = 1$. As is evident, in the averaged interference patterns, corresponding to different topological charges, the fringes at
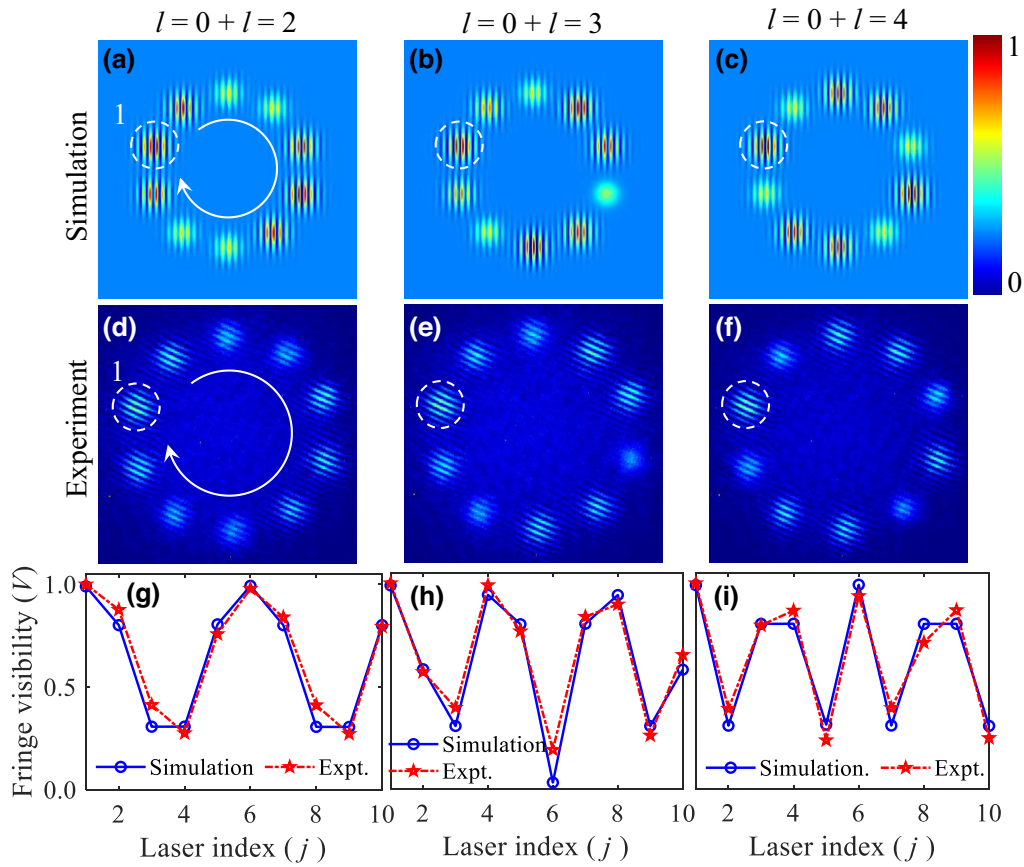
FIG. 4.   For a discrete vortex of system size $N = 10$ lasers, the determination of $l = 2$, $l = 3$, and $l = 4$. Average of interference patterns for $l = 0$ and (a),(d) $l = 2$, (b),(e) $l = 3$, and (e),(f) $l = 4$. (g)–(i) Fringe visibility as a function of laser index, corresponding to (a),(d), (b),(e), and (e),(f), respectively. The solid blue curve with circles represents the simulation and the dashed red curve with stars represents the experiment. Dashed white circles in (a)–(f) mark the locations of a selected reference laser, $j = 1$.

the lasers exhibit different behavior, and enable accurate identification of the corresponding topological charge of discrete vortices. The analyzed fringe visibility as a function of laser index (j) corresponding to $l = 11$–14 is shown in Figs. 5(i)–5(l). The phase distribution of a discrete vortex with different topological charges, formed with a 1D ring array of $N = 30$ lasers, can be given as $\phi_j = l \times (2\pi(j - 1)/30)$, where $j = 1, 2, 3, \ldots, 30$. The observed variation in the fringe visibility as a function of laser index (j) can be explained with the same reasons as given above for a discrete vortex with $N = 10$ lasers. It is clearly evidenced that the averaging of interference patterns corresponding to $l = 0 + l = 11$, $l = 0 + l = 12$, $l = 0 + l = 13$, and $l = 0 + l = 14$ leads to distinct variations in the fringe visibility as a function of laser index, and produces different numbers of dips corresponding to different values of the topological charge. For example, the averaged interference pattern corresponding to $l = 0 + l = 11$ produces 11 dips, which confirms $l = 11$ [Fig. 5(i)]. Similarly, the observation of 12, 13, and 14 dips corresponding to $l = 0 + l = 12$, $l = 0 + l = 13$, and $l = 0 + l = 14$ confirms

$l = 12$, $l = 13$, and $l = 14$, respectively. We observed excellent agreement between the simulated and experimental results, which indicates accurate determination of high-order topological charges of discrete vortices.

We also verified our method for other system sizes N, and obtained accurate values of topological charges. Our method for determining the value of the topological charge works equally well for all system sizes, for which integer values of topological charges can be defined. However, the minimum value of $N = 3$ is restricted by the definition of a discrete vortex [Eq. (14)].

So far, we have successfully shown accurate determination of the magnitude of the topological charge of a discrete vortex by averaging the interference patterns corresponding to $l \neq 0$ with the interference pattern corresponding to $l = 0$. However, with this averaging, the same results are obtained for both positive and negative values of the topological charge, and we cannot distinguish the sign of $l \neq 0$. To determine the sign of $l \neq 0$ of a discrete vortex (with known magnitude), we average its interference pattern with the interference pattern corresponding to $l = 1$
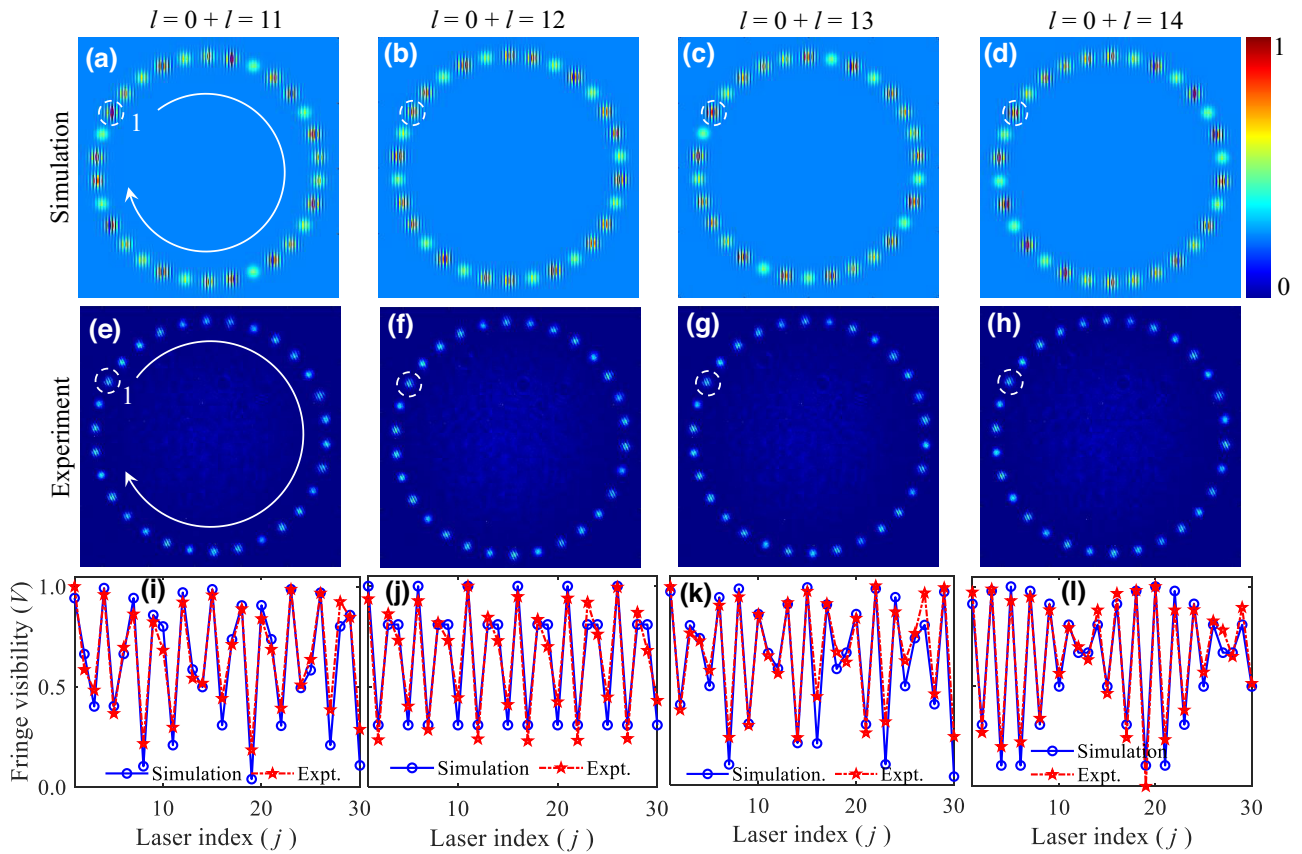
FIG. 5. Determination of higher values of the topological charge of a discrete vortex with a system size of $N = 30$ lasers. Average of interference patterns for $l = 0$ and (a),(e) $l = 11$, (b),(f) $l = 12$, (c),(g) $l = 13$, and (d),(h) $l = 14$. (i)–(l) Fringe visibility as a function of laser index, corresponding to (a),(e), (b),(f), (c),(g), and (d),(h), respectively. The solid blue curve with circles represents the simulation and the dashed red curve with stars represents the experiment. Dashed white circles in (a)–(h) mark the locations of a selected reference laser, $j = 1$.

(instead of $l = 0$ as earlier). To show this, we consider discrete vortices with different l values in a 1D ring array of $N = 10$ lasers, as shown in Fig. 6.

Figures 6(a)–6(d) show the simulated averaged interference patterns of $l = 1$, $l = 2$, $l = 3$, and $l = 4$ with $l = 1$ ($l = 1 + l = 1$, $l = 1 + l = 2$, $l = 1 + l = 3$, and $l = 1 + l = 4$). Figures 6(e)–6(h) show the simulated averaged interference patterns of $l = -1$, $l = -2$, $l = -3$, and $l = -4$ with $l = 1$ ($l = 1 + l = -1$, $l = 1 + l = -2$, $l = 1 + l = -3$, and $l = 1 + l = -4$). The dashed white circles in Figs. 6(a)–6(h) and 6(m)–6(t) represent the locations of a selected reference laser, $j = 1$. As is evident, in the averaged interference patterns corresponding to positive and negative l values with the interference pattern corresponding to $l = 1$, the fringes at the lasers appear differently, thus enabling us to distinguish the sign of the topological charge. These different interference patterns are again anticipated by the different phase distribution of discrete vortices having different topological charges. The analyzed fringe visibility as a function of laser index (j), corresponding to Figs. 6(a)–6(h), is shown in Figs. 6(i)–6(l). The dashed red curve with

circles shows the visibility curve when the interference patterns corresponding to $l = 1$, $l = 2$, $l = 3$, and $l = 4$ are averaged with the interference pattern corresponding to $l = 1$, whereas the solid blue curve with squares denotes the case when the interference patterns corresponding to $l = -1$, $l = -2$, $l = -3$, and $l = -4$ are averaged with the inference pattern corresponding to $l = 1$. As is evident, the variation of fringe visibility with laser index (j) for positive and negative l values is found to be different, and thus enables us to identify the sign of the topological charge. In particular, for $l = 1$, the fringe visibility is found to be 1 for all the lasers (no variation), and no dip is observed [dashed red curve with circles in Fig. 6(i)], whereas for $l = -1$, the fringe visibility shows variation, and two dips are observed [solid blue curve with squares in Fig. 6(i)].

As discussed earlier for Figs. 3–5, when the interference patterns corresponding to positive and negative l values are averaged with the interference pattern corresponding to $l = 0$, the number of dips in the fringe-visibility curve is found to be proportional to the magnitude of the topological charge. For example, for $l = 1$ and $l = -1$,
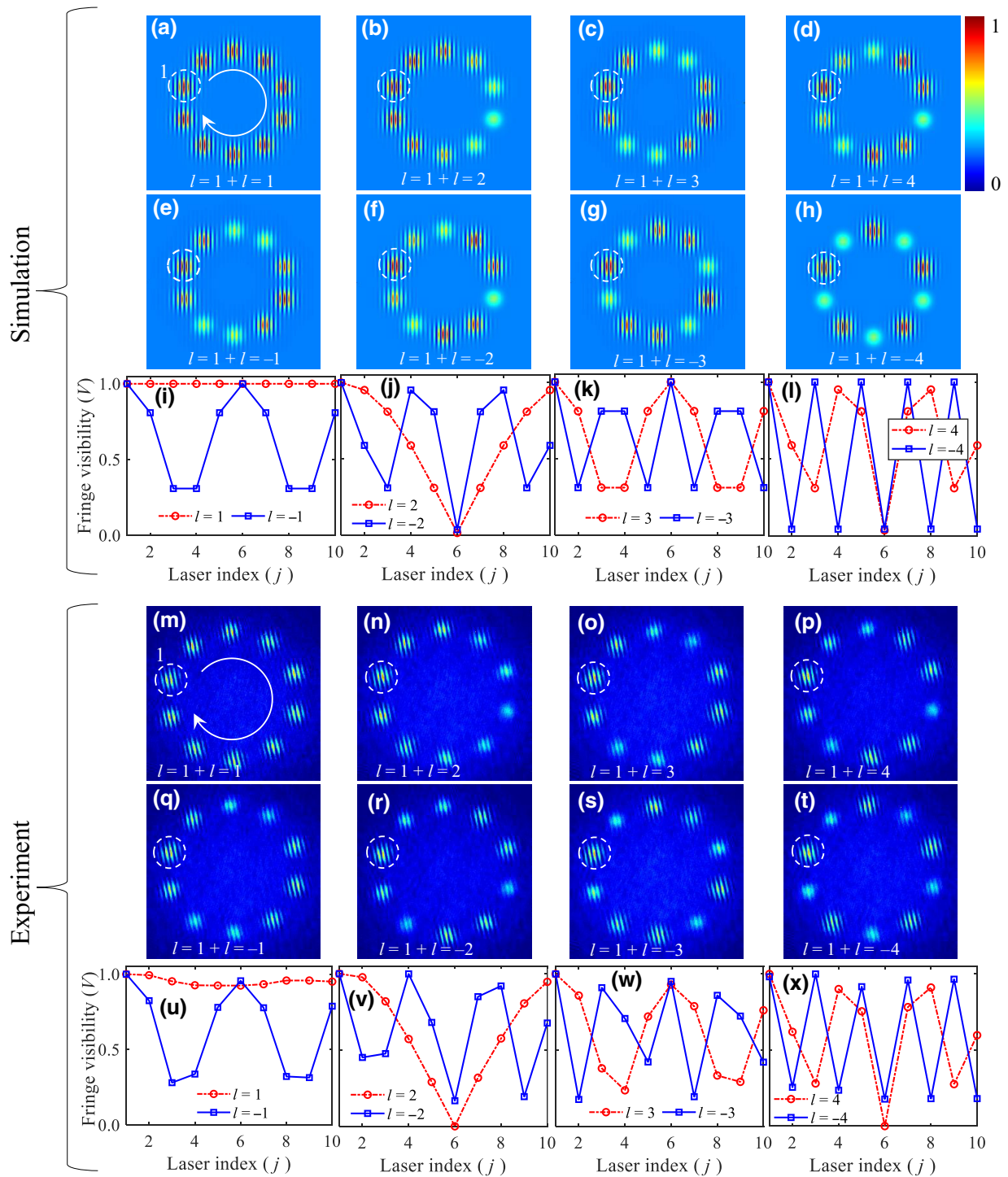
FIG. 6. Determination of the sign of the topological charge of a discrete vortex with a system size of $N = 10$ lasers. Average of interference patterns for $l = 1$ and (a),(m) $l = 1$, (b),(n) $l = 2$, (c),(o) $l = 3$, and (d),(p) $l = 4$. Average of interference patterns for $l = 1$ and (e),(q) $l = -1$, (f),(r) $l = -2$, (g),(s) $l = -3$, and (h),(t) $l = -4$. (i)–(l) Simulated results for the fringe visibility as a function of laser index, corresponding to (a),(e), (b),(f), (c),(g), and (d),(h), respectively. (u)–(x) Experimental results for the fringe visibility as a function of laser index, corresponding to (m),(q), (n),(r), (o),(s), and (p),(t), respectively. Dashed white circles in (a)–(h) and (m)–(t) mark the locations of a selected reference laser, $j = 1$.

only a single dip is observed in the fringe-visibility curve [Fig. 3(j)]. However, when the interference patterns corresponding to positive and negative l values are averaged with the interference pattern corresponding to $l = 1$, the number of dips in the fringe-visibility curve decreases by 1 for positive l values and increases by 1

for negative l values. For example, in Fig. 6(i), no dip is observed for $l = 1$ and two dips are observed for $l = -1$. Similarly, for $l = 2$, $l = 3$, and $l = 4$, one, two, and three dips, respectively, are observed [dashed red curve with circles in Figs. 6(j)–6(l)], whereas, for $l = -2$, $l = -3$, and $l = -4$, three, four, and five dips, respectively, are observed [solid blue curve with squares in Figs. 6(j)–6(l)]. This clearly indicates that the observation of a decrease (increase) in the number of dips in the fringe-visibility curve provides accurate information on the positive (negative) sign of the topological charge of a discrete vortex.

We also verified these findings experimentally; the results are shown in Figs. 6(m)–6(x). The experimental results show excellent agreement with the simulations. Thus, averaging the interference patterns corresponding to positive and negative l values with the interference pattern corresponding to $l = 1$ provides accurate information on the sign of the topological charge of a discrete vortex. This approach can be used to identify the sign of the topological charge of any order [64]. Note that the present form of our method is suitable for accurately determining the magnitude and sign of integer values of topological charges.
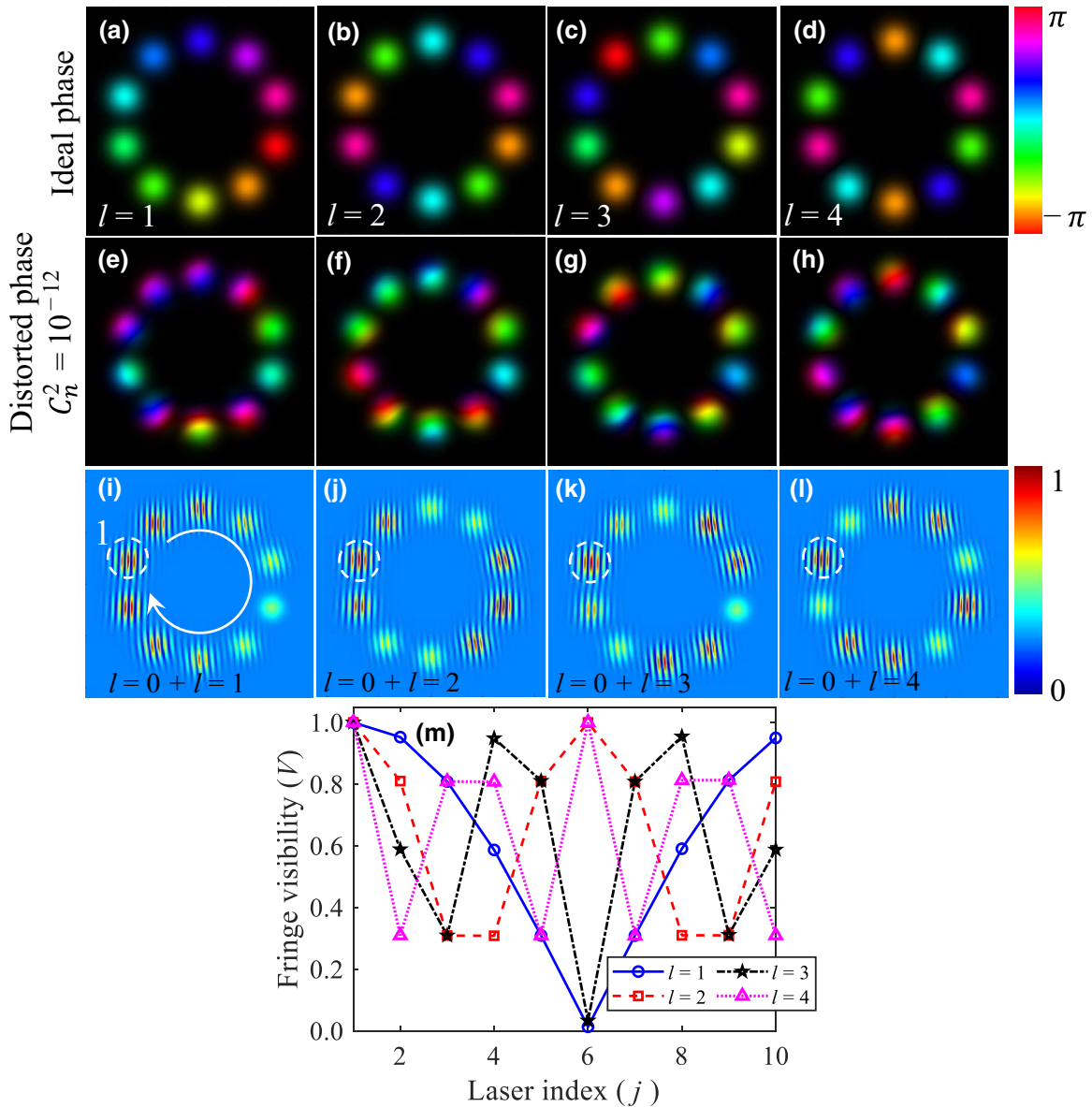

FIG. 7. Simulation results showing the effect of phase disorder on the determination of the topological charge of a discrete vortex with $N = 10$ lasers. Discrete vortex with $l = 1$–4 having (a)–(d) an ideal phase distribution and (e)–(h) a disordered phase distribution. Average of interference patterns for $l = 0$ and (i) $l = 1$, (j) $l = 2$, (k) $l = 3$, and (l) $l = 4$. (m) Fringe visibility as a function of laser index corresponding to (i)–(l). Dashed white circles in (i)–(l) mark the locations of a selected reference laser, $j = 1$.

Next we checked the robustness of our method against the phase disorder (for example, aberrations due to misalignment of optical components). We generated phase disorder in a range from $-\pi$ to π through a random phase screen using the Monte Carlo method, which behaves like a disorder medium of desired length and having disorder strength C_n^2 [65]. We considered a phase disorder with great strength $C_n^2 = 10^{-12}$. The simulated results are shown in Fig. 7. Figures 7(a)–7(d) show the ideal phase distribution of discrete vortices with $l = 1$–4 in a 1D ring array of $N = 10$ lasers. After multiplication of the phase disorder, the distorted phase distributions of discrete vortices with $l = 1$–4 are shown in Figs. 7(e)–7(h). It is clearly evident that most of the lasers in the array consist of more than a single phase.

To show whether our method can still determine accurately information on the topological charge, we measured the interference patterns of a 1D ring array of lasers with $l = 1$–4 and $l = 0$ under the same phase disorder, using Fig. 2(a). The averaged interference patterns of $l = 1$–4 with $l = 0$ are shown in Figs. 7(i)–7(l). It is evident that in the averaged interference patterns corresponding to different topological charges, the fringes at the lasers are distributed differently with different fringe visibility. Further, the orientations of the fringes at the lasers are found to be different (unlike for the ideal discrete vortices in Figs. 3 and 4). This is expected from the multiple phase structure in each laser. The analyzed fringe visibility as a function of laser index (j) for $l = 1$–4 (solid blue curve with circles for $l = 1$, dashed red curve with squares for $l = 2$, dot-dashed black curve with stars for $l = 3$, and dotted pink curve with triangles for $l = 4$) is shown in Fig. 7(m). As is evident, for different values of the topological charge, the variation in the fringe visibility consists of a different number of dips. In particular, for $l = 1, l = 2, l = 3$, and $l = 4$, one, two, three, and four dips, respectively, are found in the fringe visibility, which clearly identifies the magnitude of l values.

We also verified experimentally the effect of phase disorder on the determination of the topological charge. The results for $l = 1$–4 with the same phase disorder strength $C_n^2 = 10^{-12}$ are presented in Fig. 8. Experimentally, the phase disorder on the discrete vortex is realized by imposing random phase on the hologram along with the phase distribution of the discrete vortex [65]. Figures 8(a)–8(d) show the averaged interference patterns of $l = 1, l = 2, l = 3$, and $l = 4$ with $l = 0$ ($l = 0 + l = 1, l = 0 + l = 2, l = 0 + l = 3$, and $l = 0 + l = 4$), indicating the different fringe distribution at the lasers in each case. Corresponding to Figs. 8(a)–8(d), the analyzed fringe visibility as a function of laser index (j) is shown in Fig. 8(e). As evidenced, for $l = 1, l = 2, l = 3$, and $l = 4$, one dip (solid blue curve with circles), two dips (dashed red curve with squares), three dips (dot-dashed black curve with stars), and four dips (dotted pink curve with triangles),
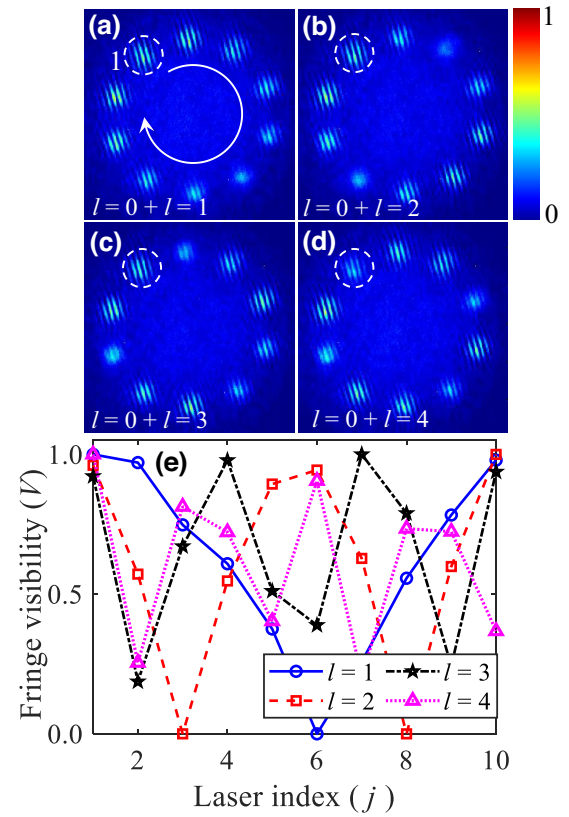

FIG. 8. Experimental results showing the effect of phase disorder on the determination of the topological charge of a discrete vortex with $N = 10$ lasers. Average of interference patterns for $l = 0$ and (a) $l = 1$, (b) $l = 2$, (c) $l = 3$, and (d) $l = 4$. (e) Fringe visibility as a function of laser index corresponding to (a)–(d). Note that the phase disorder is kept the same as in Fig. 7. Dashed white circles in (a)–(d) mark the locations of a selected reference laser, $j = 1$.

respectively, are found in the fringe-visibility variation. This clearly shows that our approach is highly robust with regard to phase disorder, as it does not affect the accurate determination of the magnitude of the topological charge of a discrete vortex. Similarly, the sign of these disordered topological charges can be determined by averaging the corresponding interference patterns with the interference pattern corresponding to disordered $l = 1$.

The numerical and experimental results show excellent agreement, and clearly indicate that our method accurately determines the magnitude and sign of the topological charge of a discrete vortex. The determination of the topological charge is not affected by imperfections such as the phase disorder caused by aberrations in the system. Further, the method can be used to determine any small to large values of the topological charge.

V. CONCLUSIONS

We have presented a new method for probing the magnitude and sign of an unknown topological charge of a

discrete vortex, which is formed by an array of lasers in 1D ring geometry. The method relies on measuring the interference pattern of a discrete vortex, which is obtained by causing a single selected reference laser to interfere with itself and with all the other lasers in a 1D ring array. The discrete laser arrays with $l = 0$ and $l \neq 0$ have different phase distributions, and thus produce interference patterns with shifted fringes. The averaging of these phase-shifted interference patterns gives rise to a variation in the fringe visibility as a function of laser index (j) in the array, thus enabling identification of the topological charge. The magnitude of the topological charge of a discrete vortex is found to be proportional to the number of dips observed in the fringe-visibility curve. After the magnitude has been determined, the sign of $l \neq 0$ can be determined by averaging the corresponding interference pattern with the interference pattern corresponding to $l = 1$. The number of dips in the fringe-visibility curve decreases by 1 for a positive topological charge and increases by 1 for a negative topological charge. Our method works well for any value of the topological charge of a discrete vortex.

Further, we verified our method against the phase disorder that may occur due to the presence of aberrations in the system. It was found that phase disorder does not influence accurate determination of the topological charge of a discrete vortex. We found excellent agreement between the experimental results and numerical simulations. In many applications, detecting the topological charge values of optical vortices, including the magnitude and sign, is crucial. Our results pave the way to precisely measure the topological charge of discrete vortices. The method can be useful in applications of discrete vortices especially where conventional continuous vortices have power limitations, such as long-range optical communication, material processing, nonlinear frequency conversion, optical trapping and manipulation, and generation of magnetic fields [3–5,11,33–35]. Thus, our work is an important step towards the future implementation of high-power discrete vortices.

Further, fractional topological charges have also attracted much attention due to their applicability, so we plan to extend our method to determine accurately fractional values of the topological charge of a discrete vortex.

APPENDIX A: PHASE HOLOGRAM FOR THE FORMATION OF A DISCRETE VORTEX IN A 1D RING ARRAY OF LASERS

To generate a discrete vortex with the desired topological charge, the phase and amplitude of the incident Gaussian beam is modulated by phase-only holograms [66]. The complex electric field of a discrete vortex can be expressed as

$$U(x,y) = A(x,y) \exp(i\phi(x,y)), \quad (A1)$$

where the amplitude $A(x,y)$ and the phase $\phi(x,y)$ take values in the intervals $[0,1]$ and $[-\pi,\pi]$. The aim is to encode the complex field $U(x,y)$ by means of a phase transmittance function (phase hologram) to incorporate amplitude variations as phase variations; that is, a function $h(x,y)$ must be given by

$$h(x,y) = \exp\left[i\psi(A,\phi)\right], \quad (A2)$$

where $\psi(A,\phi)$ accounts for both amplitude and phase variations. To find the desired form of the phase function $\psi(A,\phi)$, $h(x,y)$ can be expressed as a Fourier series in the domain of ψ as [66]

$$h(x,y) = \sum_{p=-\infty}^{\infty} c_p^A \exp(ip\phi), \quad (A3)$$

where

$$c_p^A = \frac{1}{2\pi} \int_{-\pi}^{\pi} \exp[i\psi(A,\phi)] \exp(-ip\phi)d\phi. \quad (A4)$$

The field $E(x,y)$ can be recovered from only the first-order term of Eq. (A4), provided that the following identity is fulfilled:

$$c_1^A = Ac, \quad (A5)$$

where c is a positive constant. Further, the phase function $\psi(A,\phi)$ with odd symmetry can be expressed as

$$\psi(A,\phi) = f(A)\sin(\phi). \quad (A6)$$

In this case, the phase transmittance function [Eq. (A2)] becomes $h(x,y) = \exp[if(A)\sin(\phi)]$. Expressing it in the
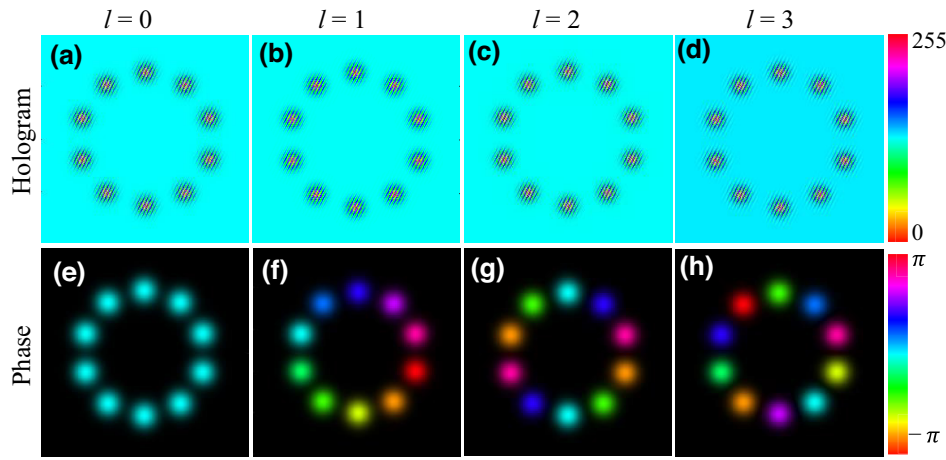
FIG. 9. Phase holograms corresponding to (a) $l = 0$, (b) $l = 1$, (c) $l = 2$, and (d) $l = 3$. Phase distributions of lasers in 1D ring array corresponding to these holograms for (e) $l = 0$, (f) $l = 1$, (g) $l = 2$, and (h) $l = 3$.

Fourier series using the Jacobi-Anger identity, we get

$$\exp[if(A)\sin(\phi)] = \sum_{q=-\infty}^{\infty} J_q[f(A)]\exp(iq\phi), \quad (A7)$$

where J_q represents a Bessel function of qth order. Using Eqs. (A3), (A5), and (A7), we get

$$c_1^A = J_1[f(A)]. \quad (A8)$$

Therefore, from Eqs. (A5) and (A8),

$$Ac = J_1[f(A)]. \quad (A9)$$

The function $f(A)$ can be determined by numerical inversion of Eq. (A9). The maximum value of c for which Eq. (A9) can be fulfilled is approximately 0.58, which corresponds to the maximum value of the first-order Bessel function $J_1(x)$, which occurs at $x \approx 1.84$. This restricts $f(A)$ to the interval $[0, 1.84]$. The modulated field consists of first and higher orders; thus, to separate the first order, a blazed grating is added to the phase of the hologram. Thus, the resultant phase will have the following form:

$$\psi = \psi(A, \phi + 2\pi N_x x + 2\pi N_y y), \quad (A10)$$

where N_x and N_y denote the grating frequencies along the x direction and the y direction, respectively. As per the requirement of the SLM, the phase of the hologram is divided into 256 levels. The spatial frequencies are chosen as $N_x = 120$ and $N_y = 60$. The holograms corresponding to $l = 0$–3 and system size $N = 10$ are shown in Figs. 9(a)–9(d), respectively. These holograms were used on the SLM to produce the desired phase distributions of lasers in a 1D ring array with $l = 0$–3, as shown in Figs. 9(e)–9(h), respectively.

A similar procedure for generating a discrete vortex for a large system size and higher topological charges is used.

APPENDIX B: FRINGE-VISIBILITY ANALYSIS

Here we present the analysis of fringe visibility in the interference patterns obtained for $l = 0$ [Fig. 3(b)] and $l = 1$ [Fig. 3(c)] as well as the corresponding averaged interference patterns. Note that the phase distribution of a discrete vortex in a ring array of $N = 10$ lasers is given as $\phi_j = l \times (j - 1)(2\pi/10)$, where $j = 1, 2, 3, \ldots, 10$ denotes the laser number in the array. The interference patterns are obtained by use of a Mach-Zhender interferometer [Fig. 2(a)], where a single selected reference laser interferes with itself and with all the other lasers in the array. The resultant interference patterns are shown in Figs. 3(d)–3(f) (simulation) and Figs. 3(g)–3(i) (experiment). The analysis of fringe visibility at all lasers in the array is shown in Fig. 10 (simulation) and Fig. 11 (experiment).

Laser $j = 1$ is a selected reference laser, where light interferes with itself, and has initial phase difference $d\phi_{1,1} = 0$ [Eq. (4)] for both $l = 0$ and $l = 1$. The interference expressions at laser 1 for $l = 0$ and $l = 1$ can be written as follows. Using Eq. (4), we find

$$I_{T1} = I_{T2} = 2I_0 [1 + \cos(0.94kx)]. \quad (B1)$$

The expression for the averaged interference pattern is given as

$$I_{\text{sum}} = \frac{I_{T1} + I_{T2}}{2} = 2I_0 [1 + \cos(0.94kx)]. \quad (B2)$$

As $d\phi_{1,1} = 0$ for both $l = 0$ and $l = 1$, so maxima and minima in the fringe pattern [Eq. (B1)] occur at the same locations [dashed red curve and dot-dashed blue curve in Figs. 10(a) and 11(a)]. In both cases, the fringe visibility V is found to be 1. The average of these two interference patterns gives no change in the fringe pattern [Eq. (B2)], and the fringe visibility V remains unchanged at 1 [solid black curve in Figs. 10(a) and 11(a)].

The interference fringes at laser 2 for $l = 0$ and $l = 1$ are obtained when the light from a selected reference laser,
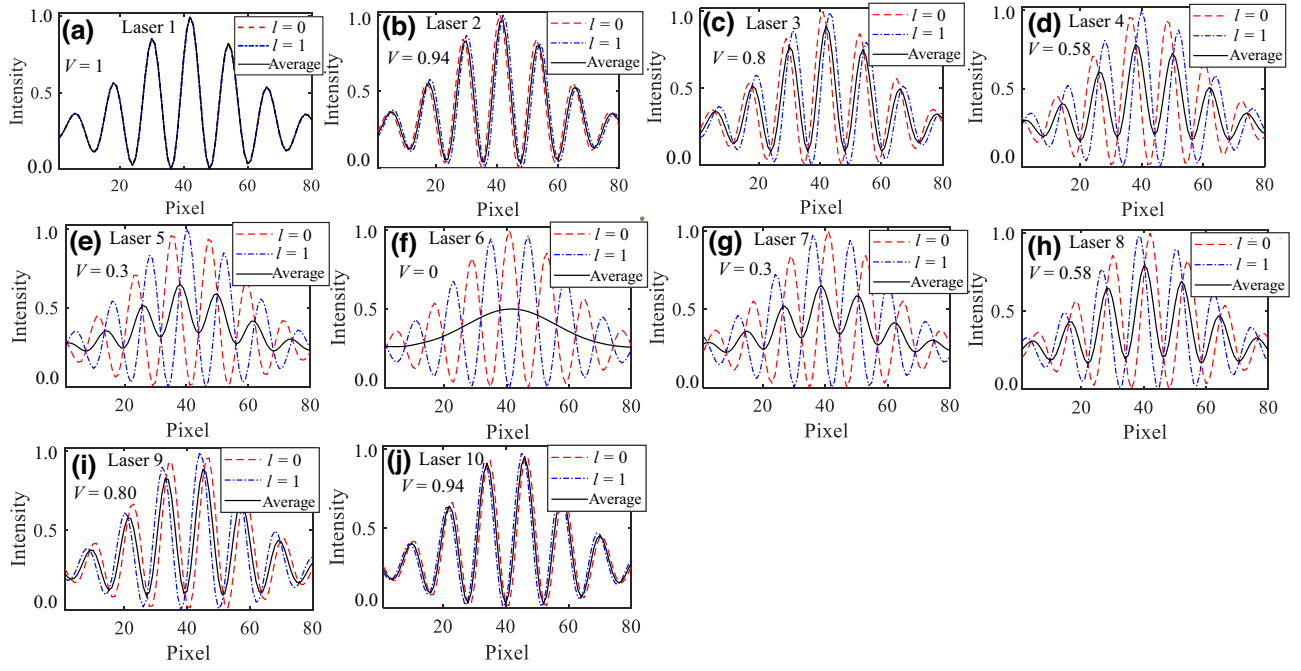
FIG. 10. Simulated results. Intensity cross section in the interference patterns for $l = 0$ and $l = 1$ and averaged interference pattern corresponding to $l = 0 + l = 1$ at (a) laser 1, (b) laser 2, (c) laser 3, (d) laser 4, (e) laser 5, (f) laser 6, (g) laser 7, (h) laser 8, (i) laser 9, and (j) laser 10. The dashed red curve denotes $l = 0$, the dot-dashed blue curve denotes $l = 1$, and the solid black curve denotes $l = 0 + l = 1$. Note that the intensity cross sections for $l = 0$ and $l = 1$ are normalized to the maximum value of 1.

$j = 1$, interferes with the light from laser $j = 2$. For $l = 0$, the initial phase difference between laser $j = 1$ and laser $j = 2$, $d\phi_{1,2}$, is zero, whereas for $l = 1$ it is $2\pi/10$. The interference expressions I_{T1} (for $l = 0$) and I_{T2} (for $l = 1$) can be given as

$$I_{T1} = 2I_0 \left[1 + \cos\left(0.94kx\right)\right], \tag{B3}$$

$$I_{T2} = 2I_0 \left[1 + \cos\left(0.94kx - 1 \times (2\pi/10)\right)\right]. \tag{B4}$$

The averaged interference pattern is given as

$$I_{\text{sum}} = I_0 \left[2 + \cos\left(0.94kx\right) + \cos\left(0.94kx - 1 \times (2\pi/10)\right)\right]. \tag{B5}$$

The interference patterns [Eqs. (B3) and (B4)] consist of fringes with clear maxima and minima, which give rise to fringe visibility $V = 1$ [dashed red curve and dot-dashed blue curve in Figs. 10(b) and 11(b)]. As is evident, in these interference patterns the fringes (maxima and minima) are shifted relative to each other, which occurs due to the different values of the initial phase difference $d\phi_{1,2}$ for $l = 0$ and $l = 1$. When these interference patterns with shifted fringes are averaged, the resultant interference pattern [Eq. (B5)] consists of fringes with reduced fringe visibility $V = 0.94$ [solid black curve in Figs. 10(b) and 11(b)].

Similarly, the interference fringes at other lasers are obtained by causing the light from a selected reference laser, $j = 1$, to interfere with the light from other lasers,

$j > 2$. In general, for $l = 0$, the phase difference between the selected reference laser, $j = 1$, and other lasers is given as $d\phi_{1,j \geq 1} = 0$, whereas in the case of $l \neq 0$, it is given as $d\phi_{1,j \geq 1} = l \times (j - 1)(2\pi/N)$, where N denotes the number of lasers in a 1D ring array. Therefore, in the case of $l = 0$, the interference fringes at lasers $j = 3, 4, \ldots, 10$ occur at exactly the same locations [dashed red curve in Figs. 10(c)–10(j) and 11(c)–11(j)]. However, in the case of $l = 1$, the interference fringes at $j = 3, 4, \ldots, 10$ occur at different locations due to different values of $d\phi_{1,j \geq 3}$ [dot-dashed blue curve in Figs. 10(c)–10(j) and 11(c)–11(j)]. Because of this, when the interference patterns at the same lasers ($j = 3, 4, \ldots, 10$) for $l = 0$ and $l = 1$ are averaged, the resultant interference pattern consists of reduced visibility [solid black curve in Figs. 10(c)–10(j) and 11(c)–11(j)]. For example, at lasers $j = 3, j = 4, j = 5$, and $j = 6$, the fringe visibility is found to be 0.8 [Figs. 10(c) and 11(c)], 0.58 [Figs. 10(d) and 11(d)], 0.3 [Figs. 10(e) and 11(e)], and 0 [Figs. 10(f) and 11(f)], respectively. For lasers $j = 7, j = 8, j = 9$, and $j = 10$, the fringe visibility is found to be 0.3 [Figs. 10(g) and 11(g)], 0.58 [Figs. 10(h) and 11(h)], 0.80 [Figs. 10(i) and 11(i)], and 0.94 [Figs. 10(j) and 11(j)], respectively. Note that a small discrepancy between the simulated and the experimental fringe visibility is expected from the small intensity difference between the lasers in the experiment. As is evident, the fringe visibility decreases monotonically for lasers $j = 1$–6 and then increases from
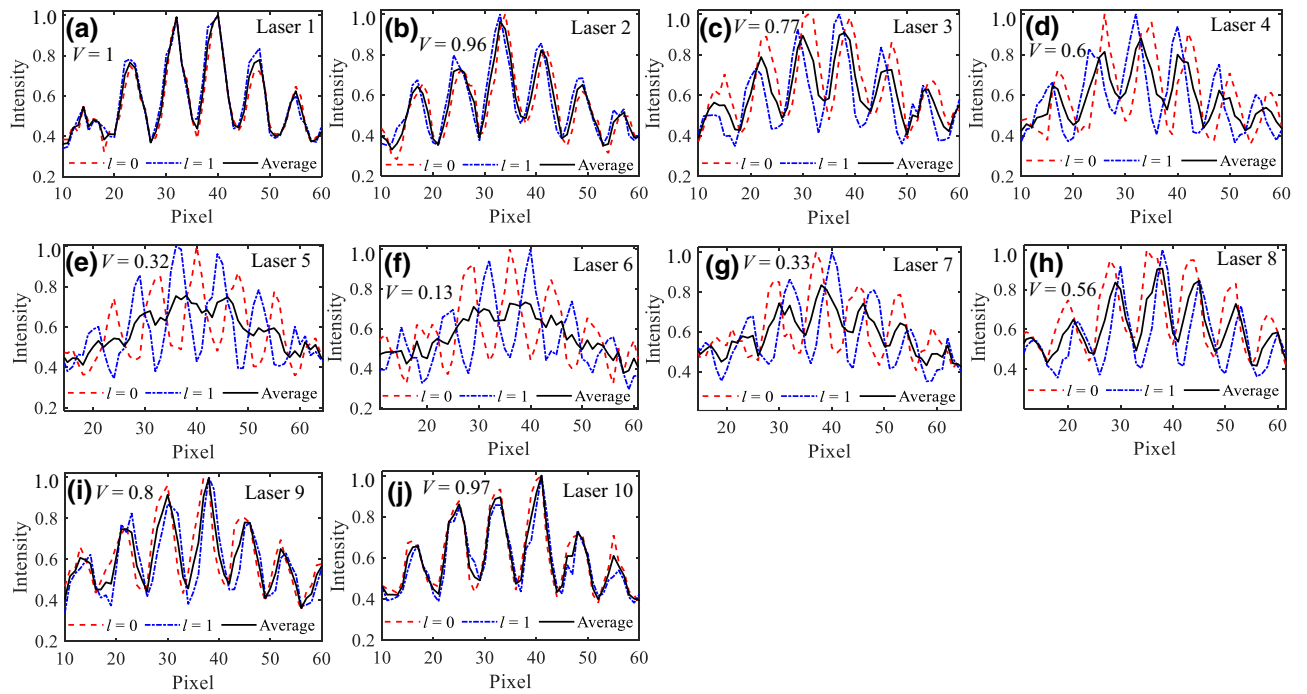
FIG. 11. Experimental results. Intensity cross section in the interference patterns for $l = 0$ and $l = 1$ and averaged interference pattern corresponding to $l = 0 + l = 1$ at (a) laser 1, (b) laser 2, (c) laser 3, (d) laser 4, (e) laser 5, (f) laser 6, (g) laser 7, (h) laser 8, (i) laser 9, and (j) laser 10. The dashed red curve denotes $l = 0$, the dot-dashed blue curve denotes $l = 1$, and the solid black curve denotes $l = 0 + l = 1$. Note that the intensity cross sections for $l = 0$ and $l = 1$ are normalized to the maximum value of 1.

laser $j = 7$ to laser $j = 10$. The increase in the fringe visibility for lasers $j = 7$–10 can be explained as follows. For laser $j = 7$, the phase difference $d\phi_{1,7} = 6 \times (2\pi/10)$, and the value of $d\phi_{1,7}$ can also be written as $[2\pi - (4 \times (2\pi/10))]$ or $[-4 \times (2\pi/10)]$. This becomes equivalent to the phase difference between laser $j = 1$ and laser $j = 5$ with the negative sign i.e., $-d\phi_{1,5}$. Note that the positive and negative values of the same magnitude $d\phi$ produce the same shift of fringes in the interference pattern, as shown in Figs. 1(a) and 1(c). The phase difference $|d\phi_{1,7}| < |d\phi_{1,6}|$ and because of this the fringe visibility in the averaged interference at laser $j = 7$ is found to be higher than for laser $j = 6$ (and same as for laser $j = 5$). Similarly, the increased values of V at lasers $j = 8$, 9, and 10 can also be explained.

APPENDIX C: DETERMINATION OF PHASES OF LASERS IN A DISCRETE VORTEX

The measured interference pattern corresponding to a discrete vortex can also be used to directly calculate the phases of the lasers by analysis of the fringe shifts with respect to a reference laser [28], which can then be used to determine the associated value of the topological charge. Direct methods have been used to determine the low-order

topological charge of a continuous vortex [61,62]. However, the direct measurement of phases of lasers may have several limitations. For example, (i) the presence of phase disorder due to imperfections and aberrations in the system can lead to distortions in the measurement of phases, and hence the topological charge of a discrete vortex may not be accurately determined; (ii) in high-order topological charge realized by a large system size N, the phase difference between neighboring lasers becomes quite small (varies as $l \times 2\pi/N$), and hence it becomes more difficult to measure these phase differences precisely, due to imperfections and aberrations in the system. So high-order topological charge may not be accurately determined by direct phase analysis.

We numerically verified the effect of phase disorder on extracting the direct phases of lasers for both small and large system sizes. From the interference pattern of a discrete vortex, the phases of the lasers are obtained by calculating the shift in the interference fringes with respect to a reference laser. The simulated results for a discrete vortex with $l = 1$ and $N = 10$ lasers are shown in Fig. 12. The solid blue curve with filled circles represents the extracted phases of lasers for an ideal discrete vortex. The red and black error bars represent the extracted phases when the system consists of low and high phase disorders, respectively. For the statistical analysis, we extracted the phases by considering 40 realizations of different
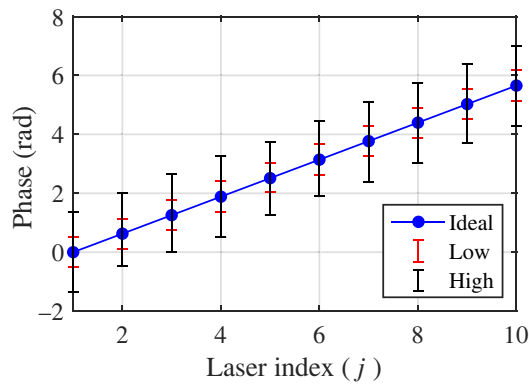
FIG. 12. For a discrete vortex with $l = 1$ and a system size of $N = 10$ lasers, the phase analysis of lasers. The solid blue curve with filled circles corresponds to an ideal discrete vortex, the red error bars correspond to a discrete vortex with low phase disorder, and the black error bars correspond to a discrete vortex with considerable phase disorder. Note that for the cases of phase disorders, the phases of the lasers are extracted from 40 different realizations.

randomness for low and high phase disorders. As is evident, when the phase disorder is introduced, the extracted phases of the lasers deviate from their ideal values. This deviation increases with the increase in phase disorder, and accordingly from the measured phases it may not be possible to accurately determine the value of the topological charge of a discrete vortex. The average root mean square error for low and high phase disorders is found to be 7% and 36%, respectively, which indicates that with considerable phase disorder it is very challenging to determine an accurate value of the topological charge of a discrete vortex (Fig. 7). Additionally, because of small phase differences between neighboring lasers, the impact of disorder becomes more noticeable when one is directly determining the phases in systems with larger sizes.

---

[1] J. Wang, J.-Y. Yang, I. M. Fazal, N. Ahmed, Y. Yan, H. Huang, Y. Ren, Y. Yue, S. Dolinar, M. Tur, and A. E. Willner, Terabit free-space data transmission employing orbital angular momentum multiplexing, Nat. Photon. **6,** 488 (2012).

[2] N. Bozinovic, Y. Yue, Y. Ren, M. Tur, P. Kristensen, H. Huang, A. E. Willner, and S. Ramachandran, Terabit-scale orbital angular momentum mode division multiplexing in fibers, Science **340,** 1545 (2013).

[3] J. Ng, Z. Lin, and C. T. Chan, Theory of Optical Trapping by an Optical Vortex Beam, Phys. Rev. Lett. **104,** 103601 (2010).

[4] M. Padgett and R. Bowman, Tweezers with a twist, Nat. Photon. **5,** 343 (2011).

[5] G. Tkachenko and E. Brasselet, Helicity-dependent three-dimensional optical trapping of chiral microparticles, Nat. Commun. **5,** 4491 (2014).

[6] S. W. Hell and J. Wichmann, Breaking the diffraction resolution limit by stimulated emission: stimulated-emission-depletion fluorescence microscopy, Opt. Lett. **19,** 780 (1994).

[7] A. Vaziri, J.-W. Pan, T. Jennewein, G. Weihs, and A. Zeilinger, Concentration of Higher Dimensional Entanglement: Qutrits of Photon Orbital Angular Momentum, Phys. Rev. Lett. **91,** 227902 (2003).

[8] Q.-F. Chen, B.-S. Shi, Y.-S. Zhang, and G.-C. Guo, Entanglement of the orbital angular momentum states of the photon pairs generated in a hot atomic ensemble, Phys. Rev. A **78,** 053810 (2008).

[9] G. Xie, H. Song, Z. Zhao, G. Milione, Y. Ren, C. Liu, R. Zhang, C. Bao, L. Li, Z. Wang, K. Pang, D. Starodubov, B. Lynn, M. Tur, and A. E. Willner, Using a complex optical orbital-angular-momentum spectrum to measure object parameters, Opt. Lett. **42,** 4482 (2017).

[10] C. Maurer, A. Jesacher, S. Bernet, and M. Ritsch-Marte, What spatial light modulators can do for optical microscopy, Laser Photonics Rev. **5,** 81 (2011).

[11] Z. Lecz, I. V. Konoplev, A. Seryi, and A. Andreev, Giga-gauss solenoidal magnetic field inside bubbles excited in under-dense plasma, Sci. Rep. **6,** 36139 (2016).

[12] A. Denoeud, L. Chopineau, A. Leblanc, and F. Quéré, Interaction of Ultraintense Laser Vortices with Plasma Mirrors, Phys. Rev. Lett. **118,** 033902 (2017).

[13] G. C. G. Berkhout and M. W. Beijersbergen, Method for Probing the Orbital Angular Momentum of Optical Vortices in Electromagnetic Waves from Astronomical Objects, Phys. Rev. Lett. **101,** 100801 (2008).

[14] M. P. J. Lavery, F. C. Speirits, S. M. Barnett, and M. J. Padgett, Detection of a spinning object using light's orbital angular momentum, Science **341,** 537 (2013).

[15] Y. Shen, X. Wang, Z. Xie, C. Min, X. Fu, Q. Liu, M. Gong, and X. Yuan, Optical vortices 30 years on: OAM manipulation from topological charge to multiple singularities, Light Sci. Appl. **8,** 90 (2019).

[16] K. Zhu, G. Zhou, X. Li, X. Zheng, and H. Tang, Propagation of Bessel-Gaussian beams with optical vortices in turbulent atmosphere, Opt. Express **16,** 21315 (2008).

[17] C. Liu, J. Liu, L. Niu, X. Wei, K. Wang, and Z. Yang, Terahertz circular Airy vortex beams, Sci. Rep. **7,** 3891 (2017).

[18] F. T. Arecchi, G. Giacomelli, P. L. Ramazza, and S. Residori, Vortices and Defect statistics in Two-Dimensional Optical Chaos, Phys. Rev. Lett. **67,** 3749 (1991).

[19] J. Schliemann and F. G. Mertens, Vortices in quantum spin systems, Eur. Phys. J. B **9,** 237 (1999).

[20] W. H. Zurek, Cosmological experiments in superfluid helium? Nature **317,** 505 (1985).

[21] L. Corman, L. Chomaz, T. Bienaimé, R. Desbuquois, C. Weitenberg, S. Nascimbene, J. Dalibard, and J. Beugnon, Quench-Induced Supercurrents in an Annular Bose Gas, Phys. Rev. Lett. **113,** 135302 (2014).

[22] T. Cookson, K. Kalinin, H. Sigurdsson, J. D. Töpfer, S. Alyatkin, M. Silva, W. Langbein, N. G. Berloff, and P. G. Lagoudakis, Geometric frustration in polygons of polariton condensates creating vortices of varying topological charge, Nat. Commun. **12,** 2120 (2021).

[23] D. N. Neshev, T. J. Alexander, E. A. Ostrovskaya, Y. S. Kivshar, H. Martin, I. Makasyuk, and Z. Chen, Observation

of Discrete Vortex Solitons in Optically Induced Photonic Lattices, Phys. Rev. Lett. **92,** 123903 (2004).

[24] B. A. Malomed and P. G. Kevrekidis, Discrete vortex solitons, Phys. Rev. E **64,** 026601 (2001).

[25] A. S. Desyatnikov, M. R. Dennis, and A. Ferrando, All-optical discrete vortex switch, Phys. Rev. A **83,** 063822 (2011).

[26] J. W. Fleischer, G. Bartal, O. Cohen, O. Manela, M. Segev, J. Hudock, and D. N. Christodoulides, Observation of Vortex-Ring "Discrete" Solitons in 2D Photonic Lattices, Phys. Rev. Lett. **92,** 123904 (2004).

[27] M. S. Petrović, S. Prvanović, and D. M. Jović, Soliton with different topological charges, Phys. Rev. A **79,** 021803 (2009).

[28] V. Pal, C. Trandonsky, R. Chriki, G. Barach, A. A. Friesem, and N. Davidson, Phase locking of even and odd number of lasers on a ring geometry: Effects of topological-charge, Opt. Express **23,** 13041 (2015).

[29] V. Pal, C. Tradonsky, R. Chriki, A. A. Friesem, and N. Davidson, Observing Dissipative Topological Defects with Coupled Lasers, Phys. Rev. Lett. **119,** 013902 (2017).

[30] V. Dev and V. Pal, Divergence and self-healing of a discrete vortex formed by phase-locked lasers, J. Opt. Soc. Am. B **38,** 3683 (2021).

[31] R. Hamerly, K. Inaba, T. Inagaki, H. Takesue, Y. Yamamoto, and H. Mabuchi, Topological defect formation in 1D and 2D spin chains realized by network of optical parametric oscillators, Int. J. Mod. Phys. B **30,** 1630014 (2016).

[32] C. N. Alexeyev, A. V. Volyar, and M. A. Yavorsky, Linear azimuthons in circular fiber arrays and optical angular momentum of discrete optical vortices, Phys. Rev. A **80,** 063821 (2009).

[33] J. Hamazaki, R. Morita, K. Chujo, Y. Kobayashi, S. Tanda, and T. Omatsu, Optical-vortex laser ablation, Opt. Express **18,** 2144 (2010).

[34] M. Duocastella and C. Arnold, Bessel and annular beams for materials processing, Laser Photonics Rev. **6,** 607 (2012).

[35] N. A. Chaitanya, A. Aadhi, M. Jabir, and G. K. Samanta, Frequency-doubling characteristics of high-power, ultrafast vortex beams, Opt. Lett. **40,** 2614 (2015).

[36] X. Chu, Q. Sun, J. Wang, P. Lü, W. Xie, and X. Xu, Generating a Bessel-Gaussian beam for the application in optical engineering, Sci. Rep. **5,** 1 (2015).

[37] D. Zhi, T. Hou, P. Ma, Y. Ma, P. Zhou, R. Tao, X. Wang, and L. Si, Comprehensive investigation on producing high-power orbital angular momentum beams by coherent combining technology, High Power Laser Sci. Eng. **7,** e33 (2019).

[38] T. Hou, Y. Zhang, Q. Chang, P. Ma, R. Su, J. Wu, Y. Ma, and P. Zhou, High-power vortex beam generation enabled by a phased beam array fed at the nonfocal-plane, Opt. Express **27,** 4046 (2019).

[39] L.-G. Wang, L.-Q. Wang, and S.-Y. Zhu, Formation of optical vortices using coherent laser beam arrays, Opt. Commun. **282,** 1088 (2009).

[40] L.-G. Wang and W.-W. Zheng, The effect of atmospheric turbulence on the propagation properties of optical vortices

formed by using coherent laser beam arrays, J. Opt. A: Pure Appl. Opt. **11,** 065703 (2009).

[41] Q. S. Ferreira, A. J. Jesus-Silva, E. J. S. Fonseca, and J. M. Hickmann, Fraunhofer diffraction of light with orbital angular momentum by a slit, Opt. Lett. **36,** 3106 (2011).

[42] J. P. C. Narag and N. Hermosa, Probing higher orbital angular momentum of Laguerre-Gaussian beams via diffraction through a translated single slit, Phys. Rev. Appl. **11,** 054025 (2019).

[43] M. P. J. Lavery, A. Dudley, A. Forbes, J. Courtial, and M. J. Padgett, Robust interferometer for the routing of light beams carrying orbital angular momentum, New J. Phys. **13,** 093014 (2011).

[44] P. Kumar, N. K. Nishchal, T. Omatsu, and A. S. Rao, Self-referenced interferometry for single-shot detection of vector-vortex beams, Sci. Rep. **12,** 17253 (2022).

[45] J. Ma, P. Li, Z. Zhou, and Y. Gu, Characteristics of fork-shaped fringes formed by off-axis interference of two vortex beams, J. Opt. Soc. Am. A **38,** 115 (2021).

[46] S. Cui, B. Xu, S. Luo, H. Xu, Z. Cai, Z. Luo, J. Pu, and S. Chávez-Cerda, Determining topological charge based on an improved Fizeau interferometer, Opt. Express **27,** 12774 (2019).

[47] S. Slussarenko, V. D'Ambrosio, B. Piccirillo, L. Marrucci, and E. Santamato, The polarizing Sagnac interferometer: a tool for light orbital angular momentum sorting and spin-orbit photon processing, Opt. Express **18,** 27205 (2010).

[48] H. I. Sztul and R. R. Alfano, Double-slit interference with Laguerre-Gaussian beams, Opt. Lett. **31,** 999 (2006).

[49] Q. Zhao, M. Dong, Y. Bai, and Y. Yang, Measuring high orbital angular momentum of vortex beams with an improved multipoint interferometer, Photon. Res. **8,** 745 (2020).

[50] P. Panthong, S. Srisuphaphon, S. Chiangga, and S. Deachapunya, High-contrast optical vortex detection using the Talbot effect, Appl. Opt. **57,** 1657 (2018).

[51] C.-S. Guo, L.-L. Lu, and H.-T. Wang, Characterizing topological charge of optical vortices by using an annular aperture, Opt. Lett. **34,** 3686 (2009).

[52] L. E. E. de Araujo and M. E. Anderson, Measuring vortex charge with a triangular aperture, Opt. Lett. **36,** 787 (2011).

[53] C.-S. Guo, S.-J. Yue, and G.-X. Wei, Measuring the orbital angular momentum of optical vortices using a multipinhole plate, Appl. Phys. Lett. **94,** 231104 (2009).

[54] S. Zheng and J. Wang, Measuring orbital angular momentum (OAM) states of vortex beams with annular gratings, Sci. Rep. **7,** 40781 (2017).

[55] Y. Guo, S. Zhang, M. Pu, Q. He, J. Jin, M. Xu, Y. Zhang, P. Gao, and X. Luo, Spin-decoupled metasurface for simultaneous detection of spin and orbital angular momenta via momentum transformation, Light Sci. Appl. **10,** 63 (2021).

[56] Y. Wen, I. Chremmos, Y. Chen, J. Zhu, Y. Zhang, and S. Yu, Spiral Transformation for High-Resolution and Efficient Sorting of Optical Vortex Modes, Phys. Rev. Lett. **120,** 193904 (2018).

[57] N. K. Fontaine, R. Ryf, H. Chen, D. T. Neilson, K. Kim, and J. Carpenter, Laguerre-Gaussian mode sorter, Nat. Commun. **10,** 1865 (2019).

[58] J. Zhou, W. Zhang, and L. Chen, Experimental detection of high-order or fractional orbital angular momentum of light

based on a robust mode converter, Appl. Phys. Lett. **108,** 111108 (2016).

[59] H.-L. Zhou, D.-Z. Fu, J.-J. Dong, P. Zhang, D.-X. Chen, X.-L. Cai, F.-L. Li, and X.-L. Zhang, Orbital angular momentum complex spectrum analyzer for vortex light based on the rotational Doppler effect, Light Sci. Appl. **6,** e16251 (2017).

[60] J. Zhurun, L. Wenjing, K. Sergiy, F. Xiaopeng, Z. Zhifeng, P. Anlian, F. Liang, D. Albert, and A. Ritesh, Photocurrent detection of the orbital angular momentum of light, Science **368,** 763 (2020).

[61] X. Hu, Z. Gezhi, O. Sasaki, Z. Chen, and J. Pu, Topological charge measurement of vortex beams by phase-shifting digital hologram technology, Appl. Opt. **57,** 10300 (2018).

[62] M. Chen, F. S. Roux, and J. C. Olivier, Detection of phase singularities with a Shack-Hartmann wavefront sensor, J. Opt. Soc. Am. A **24,** 1994 (2007).

[63] B. E. A. Saleh and M. C. Teich, *Fundamental of Photonics* (John Wiley & Sons, Hoboken, New Jersey, USA, 2007), 2nd ed.

[64] The interference pattern of a discrete vortex can have a maximum of $N/2$ dips in the fringe-visibility curve for $l = \pm N/2$, whereas for determination of the sign of $l = -N/2$, a total of $N/2 + 1$ dips are required, which is not possible, and makes it an exceptional case in our method.

[65] V. Dev, A. N. K. Reddy, A. V. Ustinov, S. N. Khonina, and V. Pal, Autofocusing and self-healing properties of aberration laser beams in a turbulent media, Phys. Rev. Appl. **16,** 014061 (2021).

[66] V. Arrizón, U. Ruiz, R. Carrada, and L. A. González, Pixelated phase computer holograms for the accurate encoding of scalar complex fields, J. Opt. Soc. Am. A **24,** 3500 (2007).